AFRL-AFOSR-VA-TR-2016-0082

Quantum control of light and matter - From the macroscopic to the nano scale

Lene Hau
HARVARD COLLEGE PRESIDENT & FELLOWS OF

02/02/2016
Final Report

Air Force Research Laboratory
AF Office Of Scientific Research (AFOSR)/ RTA1
Arlington, Virginia 22203
Air Force Materiel Command

REPORT DOCUMENTATION PAGE

Form Approved
OMB No. 0704-0188

PLEASE DO NOT RETURN YOUR FORM TO THE ABOVE ORGANIZATION.

1. REPORT DATE *(DD-MM-YYYY)*	2. REPORT TYPE	3. DATES COVERED *(From - To)*
29-01-2016	Final Performance Report	01-05-2010 - 31-10-2015

4. TITLE AND SUBTITLE
Quantum control of light and matter - From the macroscopic to the nano scale

5a. CONTRACT NUMBER

5b. GRANT NUMBER
FA9550-10-1-0208

5c. PROGRAM ELEMENT NUMBER

6. AUTHOR(S)
Hau, Lene V.

5d. PROJECT NUMBER

5e. TASK NUMBER

5f. WORK UNIT NUMBER

7. PERFORMING ORGANIZATION NAME(S) AND ADDRESS(ES)
President & Fellows of Harvard College
Office for Sponsored Programs
1033 Massachusetts Avenue, 5th Floor
Cambridge, MA 02138

8. PERFORMING ORGANIZATION REPORT NUMBER

9. SPONSORING/MONITORING AGENCY NAME(S) AND ADDRESS(ES)
Air Force Office of Scientific Research
875 N RANDOLPH ST
ARLINGTON, VA 22203

10. SPONSOR/MONITOR'S ACRONYM(S)

11. SPONSOR/MONITOR'S REPORT NUMBER(S)

12. DISTRIBUTION/AVAILABILITY STATEMENT
Distribution A, public use

13. SUPPLEMENTARY NOTES

14. ABSTRACT

We increased - by more than an order of magnitude - the storage time for coherent storage of light pulses in Bose-Einstein condensates. We can now store, sculpt, move, and revive light pulses after storage times of 0.5 minutes! We observed storage of single-photon pulses in the condensates, with unprecedented long storage times and high efficiency for storage at the single photon level. The results achieved allow for powerful processing of quantum information and for distribution of entanglement over long distances, which is essential for quantum cryptography.

We have built a compact system for integrating BECs with nanoscale structures and have developed new instrumentation and techniques for nano-fabrication. This has resulted in a unique e-beam ice-lithography setup that allows for non-destructive SEM imaging of carbon-based structures. We developed CVD methods for growing large, single-crystals of graphene and demonstrated graphene suspension over large apertures. This allows development of novel devices including chip-integrated devices for atom interferometry, of importance for navigation, and hybrid bio-graphene devices, incorporating enzymes positioned on graphene, for light-driven bio-fuel production with controlled enzymatic rates.

15. SUBJECT TERMS
Light-matter interactions; Quantum control; Slow light; Bose-Einstein condensates; Nano-science; Hybrid bio-nano systems

16. SECURITY CLASSIFICATION OF:			17. LIMITATION OF ABSTRACT	18. NUMBER OF PAGES	19a. NAME OF RESPONSIBLE PERSON
a. REPORT	b. ABSTRACT	c. THIS PAGE			19b. TELEPHONE NUMBER *(Include area code)*

Reset

Standard Form 298 (Rev. 8/98)
Prescribed by ANSI Std. Z39.18
Adobe Professional 7.0

INSTRUCTIONS FOR COMPLETING SF 298

1. REPORT DATE. Full publication date, including day, month, if available. Must cite at least the year and be Year 2000 compliant, e.g. 30-06-1998; xx-06-1998; xx-xx-1998.

2. REPORT TYPE. State the type of report, such as final, technical, interim, memorandum, master's thesis, progress, quarterly, research, special, group study, etc.

3. DATES COVERED. Indicate the time during which the work was performed and the report was written, e.g., Jun 1997 - Jun 1998; 1-10 Jun 1996; May - Nov 1998; Nov 1998.

4. TITLE. Enter title and subtitle with volume number and part number, if applicable. On classified documents, enter the title classification in parentheses.

5a. CONTRACT NUMBER. Enter all contract numbers as they appear in the report, e.g. F33615-86-C-5169.

5b. GRANT NUMBER. Enter all grant numbers as they appear in the report, e.g. AFOSR-82-1234.

5c. PROGRAM ELEMENT NUMBER. Enter all program element numbers as they appear in the report, e.g. 61101A.

5d. PROJECT NUMBER. Enter all project numbers as they appear in the report, e.g. 1F665702D1257; ILIR.

5e. TASK NUMBER. Enter all task numbers as they appear in the report, e.g. 05; RF0330201; T4112.

5f. WORK UNIT NUMBER. Enter all work unit numbers as they appear in the report, e.g. 001; AFAPL30480105.

6. AUTHOR(S). Enter name(s) of person(s) responsible for writing the report, performing the research, or credited with the content of the report. The form of entry is the last name, first name, middle initial, and additional qualifiers separated by commas, e.g. Smith, Richard, J, Jr.

7. PERFORMING ORGANIZATION NAME(S) AND ADDRESS(ES). Self-explanatory.

8. PERFORMING ORGANIZATION REPORT NUMBER. Enter all unique alphanumeric report numbers assigned by the performing organization, e.g. BRL-1234; AFWL-TR-85-4017-Vol-21-PT-2.

9. SPONSORING/MONITORING AGENCY NAME(S) AND ADDRESS(ES). Enter the name and address of the organization(s) financially responsible for and monitoring the work.

10. SPONSOR/MONITOR'S ACRONYM(S). Enter, if available, e.g. BRL, ARDEC, NADC.

11. SPONSOR/MONITOR'S REPORT NUMBER(S). Enter report number as assigned by the sponsoring/ monitoring agency, if available, e.g. BRL-TR-829; -215.

12. DISTRIBUTION/AVAILABILITY STATEMENT. Use agency-mandated availability statements to indicate the public availability or distribution limitations of the report. If additional limitations/ restrictions or special markings are indicated, follow agency authorization procedures, e.g. RD/FRD, PROPIN, ITAR, etc. Include copyright information.

13. SUPPLEMENTARY NOTES. Enter information not included elsewhere such as: prepared in cooperation with; translation of; report supersedes; old edition number, etc.

14. ABSTRACT. A brief (approximately 200 words) factual summary of the most significant information.

15. SUBJECT TERMS. Key words or phrases identifying major concepts in the report.

16. SECURITY CLASSIFICATION. Enter security classification in accordance with security classification regulations, e.g. U, C, S, etc. If this form contains classified information, stamp classification level on the top and bottom of this page.

17. LIMITATION OF ABSTRACT. This block must be completed to assign a distribution limitation to the abstract. Enter UU (Unclassified Unlimited) or SAR (Same as Report). An entry in this block is necessary if the abstract is to be limited.

Final Report

Lene V. Hau

FA9550-10-1-0208

Quantum control of light and matter – From the macroscopic to the nano scale

In our experiments, we stop and extinguish light pulses in a Bose Einstein condensate (BEC). Optical information imprinted in the light pulse is stored and manipulated by converting the light pulse into a small atom pulse that is a perfect matter copy of the extinguished light pulse. The matter copy can be moved around and reshaped, and after it enters a second (or the same) BEC, the light pulse can be revived; phase locking induced by the presence of the condensate helps convert the information from the matter copy to the optical field. The matter copy can be trapped – stored - for extended time scales and reshaped in whatever form required. The induced changes will then be present in the revived light pulse.

Using and developing these methods under this grant, we have increased - by more than an order of magnitude - the storage time for coherent storage of light pulses in Bose-Einstein condensates (BECs). We can now store, sculpt, move, and revive light pulses after storage times of 0.5 minutes! We have also successfully implemented and observed storage of single-photon pulses in the condensates, with unprecedented long storage times and high storage efficiency for storage at the single photon level. This will be described in more detail below.

These experiments give us an unprecedented ability to manipulate quantum information. The results achieved allow for powerful processing of quantum information with BECs

and for distribution of entanglement over long distances, which is essential for quantum cryptography.

During the grant period, we have also designed and built a new, ultra-compact system for integrating BECs with nanoscale structures, including graphene-based structures. As part of this project, new instrumentation and techniques have been developed for fabrication of novel nanoscale structures. A unique new setup for e-beam ice-lithography has been built in our lab. This significantly enhances the infrastructure available at Harvard for nanofabrication, and allows for SEM imaging of carbon-based nanoscale structures - carbon nanotubes and graphene, for example. During imaging, the nano-structures are protected by a thin layer of ice against contamination with amorphous carbon that would otherwise build up on the structures during their exposure to the electron beam. This in turn allows, for example, for positioning and deposition, with nanometer precision, of electrical contacts for device fabrication. In parallel, we have developed a fabrication facility for growing large, single-crystal grains of graphene with chemical vapor deposition. We have also demonstrated the successful suspension of such pristine, single crystals of mono- and multilayer graphene over the largest-area apertures in an insulating substrate ever reported. These facilities and results have important applications for the development of novel devices, including uniquely sensitive atom detectors such as chip-integrated devices for atom interferometry, which is of importance for precise navigation. They also include hybrid bio-graphene devices incorporating enzymes positioned on graphene for dynamic control of enzymatic reactions and for sensitive detection of bio and organic molecules.

The Bose-Einstein condensate: An efficient quantum memory for long-term storage

Principal Investigator: Lene Vestergaard Hau
Postdoctoral Researcher: Rui Zhang
Graduate Student: Evan Daniel Walsh

Quantum information science has great potential for driving future technologies. In particular, quantum cryptography and quantum computation can attain unprecedented communication security and computation power for specified tasks. Single photons are ideal quantum-information carriers, as they can be transmitted in optical fibers with low loss. However, they are not ideal for information processing due to the weak non-linear interactions usually present at the single-photon level. Therefore, applications will rely heavily on the use of quantum memory, where quantum optical states can be stored in matter form, processed, and later retrieved. Indeed, one of the biggest challenges for quantum information science is the development of a quantum memory that allows for long storage times and for low loss during photon storage and retrieval. Under this grant, we have demonstrated the first quantum memory that combines high efficiency (>50%) with an unprecedented long storage time (300ms) for light storage at the single photon level. The system furthermore allows for multi-mode storage.

Experimental implementations of a quantum memory with high-efficiency (> 50%) optical storage and read-out have been achieved [1-7], but the longest demonstrated storage times in these systems are just a few milliseconds [3, 8]. To distribute quantum entanglement over hundreds of kilometers, as needed in quantum networks [9], repeaters

are needed that require quantum memory with storage times of hundreds of milliseconds[10]. Although a storage time of close to 100ms for a single atomic excitation was observed[11], the efficiency of the subsequent conversion to a single-photon was only 16%, corresponding to an efficiency of just *a few percent* for a full optical read-in/out operation. Under this grant, we have experimentally demonstrated a BEC based quantum memory with total conversion efficiency > 50% and storage times of up to 300 ms. Importantly, we have also demonstrated multiple-pulse storage and deterministic reordering of the output-pulse sequence.

We use slow and stopped light in a Bose-Einstein condensate (BEC) to achieve this[12,,13]. When photon pulses enter the BEC, they are mapped onto matter wave excitations. The combination of high atom-number density and optical density (OD) of a BEC allows a photon pulse to be spatially compressed, contained, and converted to a matter imprint within the condensate. The off-diagonal long range order of a BEC and the stimulated Bosonic-matter-wave scattering, that can be induced by a condensate, allow for photon pulse revival after long-term storage.

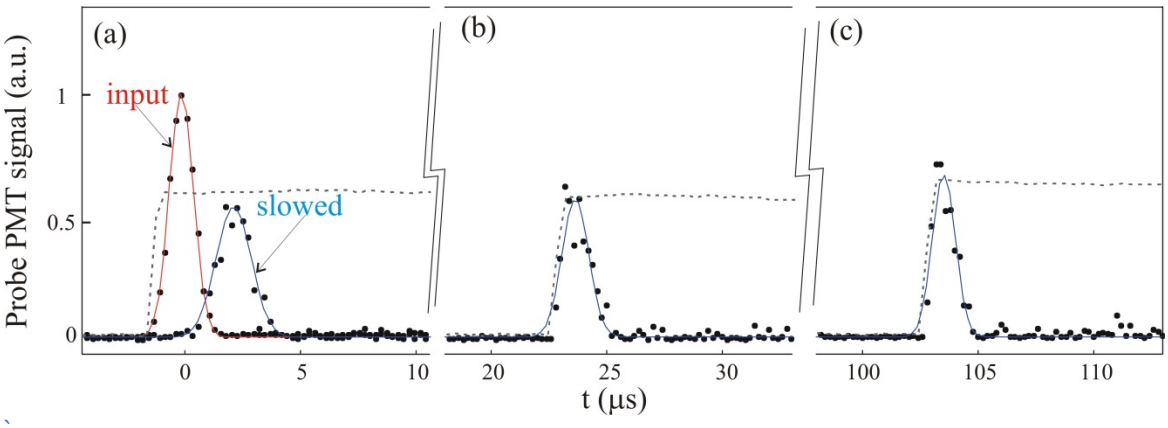

Figure 1. Efficient storage of a light pulse with 30,000 photons. (**a**) A probe pulse is injected and slowed in a BEC 6 ms after the condensate is released from an optical dipole trap. With a photomultiplier tube

(PMT), we measure a 65 % transmission through the BEC and a pulse delay of 2.3 μs. (A co-propagating coupling laser field illuminates the condensate; its timing is shown by the dashed curve.) (**b**) For longer delays, the coupling field is turned off when the input pulse is slowed, spatially compressed, and contained within the BEC. A matter-wave imprint of the slowed pulse will then remain stored in the BEC. The coupling field is turned back on after 23 μs of storage and the pulse is revived, resulting in an overall memory efficiency of 60%. (**c**) For 103 μs storage, the efficiency is the same.

Our experimental setup for creating BECs has been described previously [14]. To first illustrate that high conversion efficiency is possible, we performed the experiment illustrated in Fig. 1. Optical 'probe' pulses are sent into a BEC after the dipole trapping potential is turned off and the condensate has expanded freely for 6 ms. As shown in Fig.1a, 65% of an input light pulse is slowed and transmitted by the BEC in the presence of a co-propagating 'coupling' laser beam. Figs. 1b-c show that the input pulse can be stored for 100 μs and retrieved with negligible additional loss.

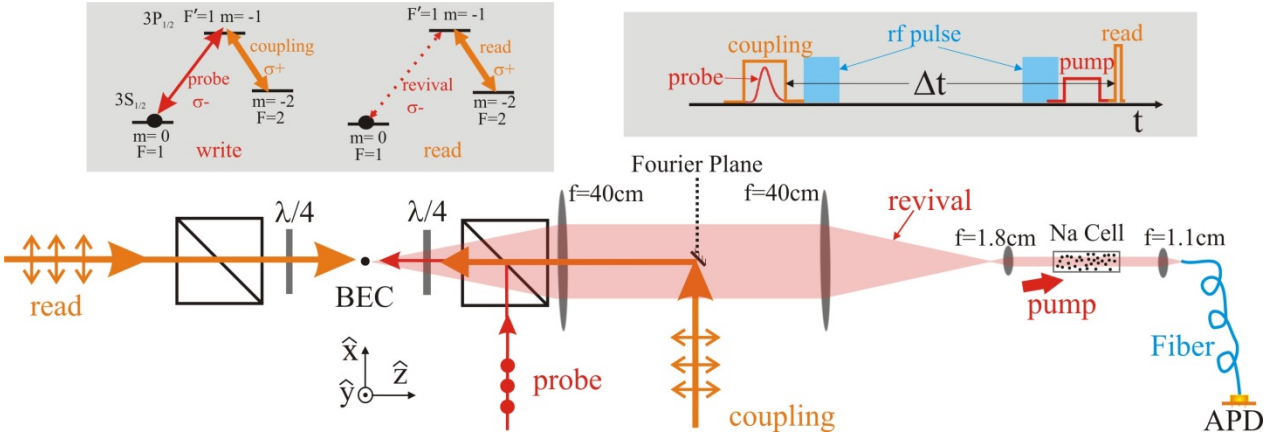

Figure 2. Experimental setup, atomic transition diagram, and time sequence of the experiment. The input probe pulse and coupling beam are injected from polarization maintaining fibers while the read beam is free-space coupled. All have Gaussian spatial profiles (waists are 1.8 mm, 0.4 mm, and 1.0 mm, respectively, at the location of the BEC). The probe pulse is temporally Gaussian shaped (HWHM of 750 ns) while the coupling (read) beam is a 2.6 μs (120 ns) square pulse. The peak Rabi frequency of the coupling (read) beam is 12.5 MHz (29.5 MHz), and the peak intensity of the probe pulse is 2×10^{-5} mW/cm^2 for storage at the single photon level. The probe and coupling fields are 40 MHz detuned while the read beam is on resonance.

Next, to achieve long storage times, the BEC has to remain trapped. In order to minimize optical propagation losses in the condensate, we use the experimental setup of

Fig. 2. The host BEC is in the |F=1, m=0> internal state. For the "write" procedure (storage of input probe pulse), the probe and coupling beams are co-propagating in the negative z-direction. When the coupling beam is turned off, the matter wave excitation created by the input pulse remains as an atomic imprint in state |F=2, m=-2>. After some storage time, a "read" laser beam that propagates in the positive z-direction is sent in, thus converting the atomic imprint back to the optical field. The optical output mode travels in the positive z-direction with a mode profile determined by the atomic matter imprint before revival. The output pulse exits the BEC immediately (without the need to propagate through the entire condensate) and is coupled into a 62 μm-core multimode fiber and guided to an avalanche photodiode (APD) where individual photons of the output mode are detected.

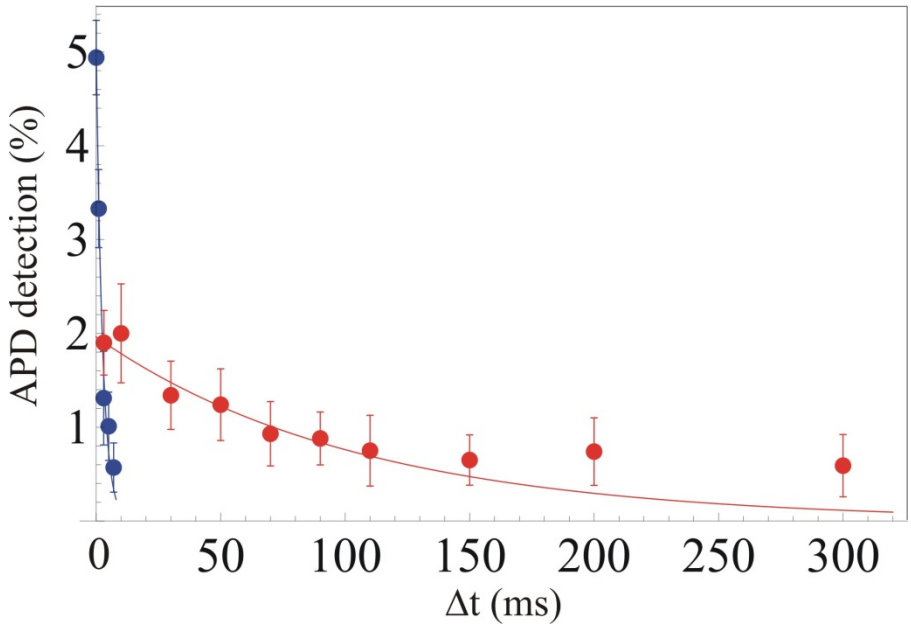

Figure 3 Photon revival as a function of storage time for single-photon coherent input pulses. The input pulses have a mean photon number of 1.0 within the cross-sectional area of the BEC. Blue dots: experimental data for stored imprints in the |F=2, m=-2> state; storage times from 100 μs to 7 ms. Red dots: experimental data for imprints transferred to and stored in the |F=1, m=-1> state; storage times from 3 ms to 300 ms. The curves are fits to exponential functions with decay times of 2.6±0.3 ms (blue) and 106±10 ms (red). In the latter case, the fit is to data for storage times below 110 ms only, and it is clearly seen that a much larger decay time is achieved for storage times above 110 ms. The data are shown after

subtraction of a noise level of 0.29% (measured without injection of probe pulses). Error bars represent the standard deviation.

We first test the memory with single-photon coherent input pulses. The write and read procedure is repeated typically 50 times for each BEC, which is held in the dipole trap for 5.6 seconds. (During this time the number of condensate atoms is reduced by 40 % from collisions with background atoms.) We record the number of APD counts that — after noise reduction and division by the total number of repetitions — results in the APD detection percentages plotted in Fig. 3 as a function of storage time (blue dots). (Each data point is a result of accumulated counts for over 100 BECs, for a total of roughly 5000 repetitions of the experiment.) In the figure, we show a fit of the data to an exponential decay curve with a 1/e decay time of 2.6ms. At 100 μs storage time, the APD detection percentage of 5.0±0.4% corresponds to 0.53±0.04 revived photons per 1.0 photon input, i.e., a total conversion efficiency for this condensate-based memory of 53±4%. (Here we take into account an 83% optical transmission loss from right after the BEC to the APD [including a 58% loss through the Na vapor cell] and a 55% detection efficiency of the APD.)

The lifetime of 2.6 ms is limited by collisions between the host condensate (in |F=1, m=0>) and the atomic imprint (in |F=2, m=-2>). To increase the lifetime, we transfer the atomic imprint to another internal state via an adiabatic-rapid-passage (ARP) process. An RF pulse of 1 ms duration is applied to the atoms right after the write process, and the RF frequency is swept through a range of 40 kHz centered around 1.7 GHz. (A bias magnetic field of 9 G is applied along the z-direction.) The imprint is transferred coherently from |F=2, m=-2> to the |F=1, m=-1> state where it suffers no loss from collisions with the

host condensate (ARP efficiency is >95%). Right before the read process, another ARP pulse transfers the atomic imprint back to |F=2, m=-2>. The result is a much longer memory time as shown in Fig. 3 (red dots). The data, for storage times below 110 ms, are fitted to a 1/e decay time of 106 ms.

The shortest storage time recorded with use of the ARPs is 3 ms, which roughly corresponds to the duration of the two ARP pulses and is comparable to the lifetime of the |F=2, m=-2> state. By decreasing the RF pulse length to roughly 100 μs, we could increase the efficiency for all storage times by a factor of 2.5 above the values shown by the red dots in Fig. 3. (This would require an increased RF field strength beyond what we can achieve in our current setup. The RF antenna inside the vacuum chamber was designed for fields in the MHz frequency range, used during the evaporative cooling process, so the impedance matching at 1.7 GHz is rather poor.)

Fig. 3 (red dots) shows that the decay for storage times above 110 ms is much slower than for shorter storage times. To investigate this, we apply input probe pulses with 100,000 photons to allow for simultaneous observations of the dynamics of the atomic imprints during storage.

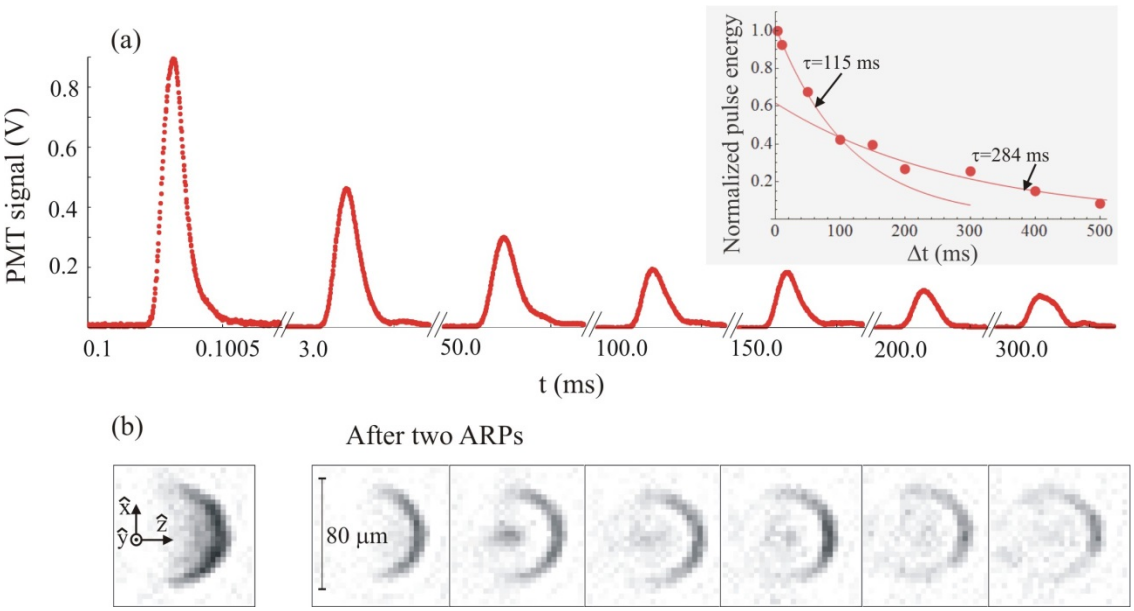

Figure 4. Pulse revival and matter-wave-excitation dynamics. (**a**) Revived optical outputs after storage of input probe pulses, each with 100,000 photons, for storage times of 100 μs to 300 ms. The experimental setup is the same as in Fig. 2 except that the APD is replaced by a photo-multiplier tube (PMT). Each pulse shown is the average over 3 trials. For 3 ms or longer, two ARPs are applied. The output pulse energy as a function of storage time (above 3 ms) is shown in the inset. There are clearly two time constants for the decay: a decay time of 115 ms for storage times below 100 ms, and a decay time of 284 ms for storage times above 100 ms. (**b**) Images of the corresponding atomic imprints recorded just before they are converted to light. For each image, the storage time is the same as for the revived pulse above.

Fig. 4 (a) shows optical pulses revived after different storage times with the corresponding atomic imprints (no read beam) shown in Fig 4 (b). The decay data (inset) agree well with the single photon decay data in Fig. 3, and for storage times above 100 ms, we fit to a decay time of 284ms. Based on the observed dynamics of the atomic imprints, we believe that the faster initial decay is due to the fact that a small part of an imprint slides and disperses along the upper and lower surfaces of the condensate (roughly parallel to the x-z plane), as shown by the dark center spot in the 50ms picture. The major part of the imprint, though, stays located - trapped close to the outer (+z) edge of the condensate by a combination of a repulsive interaction with the host condensate

and the dipole trap. Thus, by spatially limiting the size of the input pulse in the y direction, the memory lifetime would be extended.

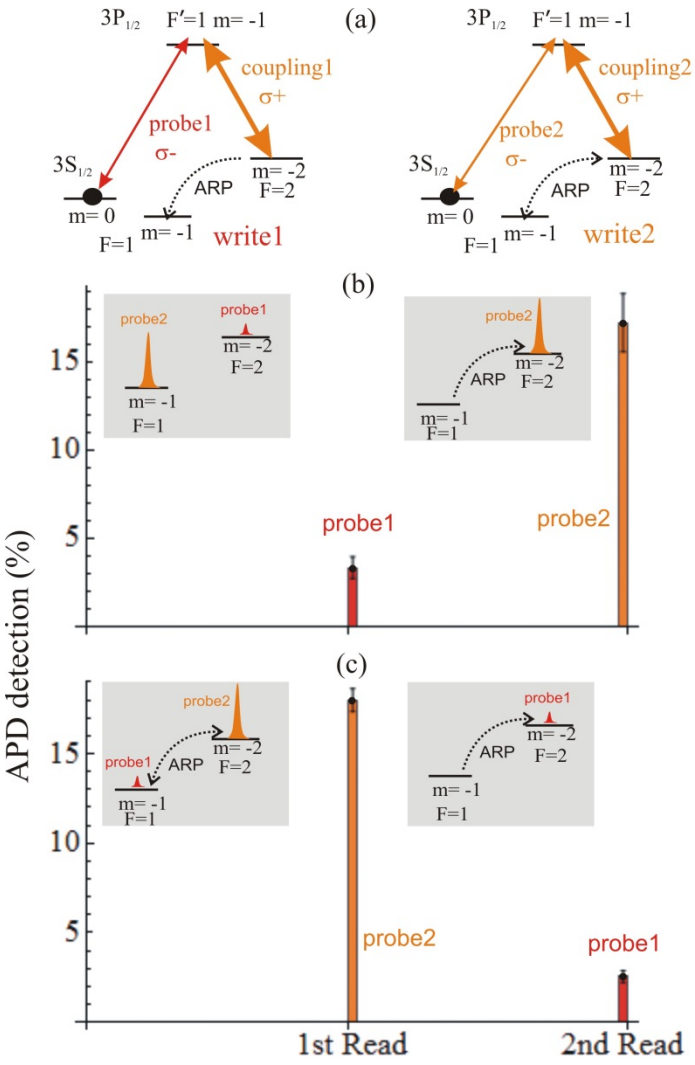

Figure 5. Two-pulse storage. (**a**) After creating an atomic imprint with the "write1" procedure, and coherently transferring the atomic amplitude to |F=1, m=-1> with an ARP, we inject a second input pulse ("write2") to form a second imprint, in |F=2, m=-2>. Another ARP is now applied leaving the first imprint in |F=2, m=-2> and the second imprint in |F=1, m=-1>. **(b)** Pulses are read out in the same order as they were read in, by applying a read beam followed by an ARP and another read beam. (**c**) Reversed output pulse sequence with application of an additional ARP before the first read beam. With the host BEC in the |F=2> state, the quantum memory could store five distinct input pulses. For Na atoms, the |F=2, m=-2> and |F=1, m=0> states can coexist for as long as 1 s at 132 G magnetic field[14]. For Rb, they have long lifetimes at 15 G.

We have confirmed that the BEC-based memory preserves strong non-classical quantum correlations and have measured a cross-correlation function of g_{12} =48±12 >>2

(see Methods). Furthermore, we have demonstrated that multi-mode storage is possible with use of the experimental sequence shown in Fig. 5a. After creating an atomic imprint with a first input pulse and coherently transferring the imprint to another, protected internal state via an ARP, a second input pulse is injected to form a second imprint. Both input pulses have a mean photon number of 9. To easily distinguish the pulses after read out, we store the imprints for 8 ms. After this time, the mean atom number in one of the imprints has decreased to 1.3, whereas the second-pulse imprint has the mean-atom number of 6.6. We can choose to read the pulses out in the same order as they were read in (Fig. 5b), or reverse the output pulse sequence by applying an additional ARP before the first pulse is read out (Fig.5c).

In summary, we have demonstrated that a BEC works as an efficient quantum memory for long-term storage of optical pulses, and that multiple-pulse storage is possible with a pulse sequence at read-out that is fully controllable. Utilizing the memory in quantum repeater architectures will allow an extension of remote entanglement in quantum networks to distances of several hundreds of kilometers [10]. The controlled read-out of multiple pulses also enables select atomic excitations to be stored in protected states (not disturbed by the read laser), which is of great importance for implementation of temporally multiplexed quantum repeaters [15] that can greatly increase the success rate for achieving remote entanglement. Finally, with use of the demonstrated two-pulse storage scheme, the proposed photon-photon phase gate [16] can be realized with a significantly simplified setup.

Methods

Experimental setup. A 1 mm gold-coated silicon chip is placed at the center of the Fourier plane of the f=40 cm imaging lens system (Fig. 2). The chip acts as a mirror for injection of the coupling beam and as a beam blocker for the 0.1 % of the read beam that is not coupled out by the second polarization beam splitter along the beam path, thus reducing the read noise. To further suppress this noise, a Na vapor cell filled with a 10 Torr neon buffer gas is used. Before each read pulse, a "pump" laser illuminates the heated cell to pump Na atoms of the cell from states F=1 to F=2. The pumped atoms absorb the remaining part of the read beam but allow transmission of the revived probe photons. To minimize background counts, the APD is gated such that photons are detected only during the time the read beam is on. The position of the BEC can vary by ±10 μm in the x direction and by ±5 μm in y due to some residual instability of the optical-dipole trapping beams. (The size of the trapped BEC is about 80 μm along x and z, and 15 μm along y.) The imaging system maps a disk of 101 μm diameter at the location of the BEC onto the core of the multimode fiber shown. Therefore the position fluctuation of the BEC will not result in signal loss at the APD.

Cross-correlation measurement. To confirm that the BEC-based memory supports non-classical quantum correlations, we have used a method similar to that in reference [17], and the transition diagram is the same as in Fig. 2. A weak write pulse, detuned 20 MHz from the probe transition, illuminates the BEC and generates a Stokes photon on the coupling transition. At the same time, one atomic excitation is created in the $|F=2, m=-2\rangle$ state. The resulting matter wave mode with the single atomic excitation is stored for 20 μs and then illuminated by a read beam and converted to an anti-Stokes optical mode,

with a single photon, by the same revival method as used above. We measure the cross-correlation function for the Stokes and anti-Stokes modes and observe strong quantum correlations with a measured g_{12} =48±12 >>2. (For this quantum correlation measurement we have used a relatively short storage time of 20 μs to allow accumulation of good statistics on reasonable timescales, and a magnetic field of B=132G is present in the z-direction to minimize the collision-induced loss of atomic excitations.)

The write pulse is 30 ns long and has a peak intensity of 0.1 mW/cm^2. The read pulse is 90 ns long, on resonance with the coupling transition, and has a peak intensity of 5 mW/cm^2. The Stokes photons are collected by two one-inch diameter, f=50cm imaging lenses and the photon mode is then shaped by two cylindrical lenses (f_x=15 cm, f_y=5 cm). Finally an f=1.1 cm lens focuses the Stokes mode onto a 3 μm-core single-mode optical fiber to direct the photons to the detector (APD_1). We use a different set of lenses and fiber system here than that shown in Fig. 2 to reduce the noise counts. Whether or not we detect a Stokes photon, a read pulse is sent in and a gate pulse is applied to the anti-Stokes detector (APD_2). The anti-Stokes photons pass through a similar lens/fiber system to APD_2, except with the addition of a Na vapor cell to reduce noise from the read beam, and the Stokes and anti-Stokes fields are mode-matched to each other. To avoid excessive write (read) photons leaking into the APD_1 (APD_2), we choose an angle of about 1.2 degrees between the propagation directions of the write (read) and Stokes (anti-Stokes) fields. The outputs of the APDs are sent to a field-programmable gate array (FPGA). The number of clicks from each APD is registered and recorded by the FPGA and sent to the computer.

The cross-correlation function is $g_{12}=p_{12}/p_1p_2$, where p_{12} is the joint detection probability for detecting both a Stokes and an anti-Stokes photon, and $p_1<<1$ (p_2) the probability for detecting a Stokes (anti-Stokes) photon. By dividing the number of clicks from APD_1 (APD_2) with the total number of trials (total number of write or read pulses sent to the BEC), we can get the probability p_1 (p_2). The FPGA also counts the number of joint detections with APD_1 and APD_2 (i.e., clicks from both APDs for the same trial with the write and read procedure). This number divided by the total number of trials is p_{12}. For each BEC, the write and read procedure is repeated 15,000 times. With a total number of trials $N=3\times10^6$, APD_1 registered 1196±110 clicks, APD_2 registered 1057±120 clicks, and 20±5 joint detections were recorded. This gives the value of g_{12} mentioned above.

References

1. Hedges, M. P., Longdell, J. J. , Li, Y. & Sellars, M. J. Efficient quantum memory for light, *Nature,* **465**, 1052-1056 (2010).

2. Hosseini, M. *et al*. Unconditional room-temperature quantum memory, *Nature Phys.* **7**, 794-798 (2011).

3. Bao, X.-H. *et al*. Efficient and long-lived quantum memory with cold atoms inside a ring cavity, *Nature Phys.* **8**, 517-521 (2012).

4. Riedl, S. *et al*. Bose-Einstein condensate as a quantum memory for a photonic polarization qubit, *Phys. Rev. A,* **85**, 022318 (2012).

5. Sparkes, B. M. *et al*. Gradient echo memory in an ultra-high optical depth cold atomic ensemble, *New J. Phys.* **15**, 085027 (2013).

6. Chen, Y.-H. C. *et al*. Coherent optical memory with high storage efficiency and large fractional delay, *Phys. Rev. Lett.* **110**, 083601 (2013).

7. Sabooni, M., Li, Q., Kröll, S. & Rippe, L. Efficient quantum memory using a weakly absorbing sample, *Phys. Rev. Lett.* **110**, 133604 (2013).

8. Xu, Z. *et al*. Long lifetime and high-fidelity quantum memory of photonic polarization qubit by lifting Zeeman degeneracy, *Phys. Rev. Lett.* **111**, 240503 (2013).

9. Kimble, H. J. The quantum internet, *Nature,* **453**, 1023-1030 (2008).

10. Sangouard, N., Simon, C., Riedmatten, H. d. & Gisin, N. Quantum repeaters based on atomic ensembles and linear optics, *Rev. Mod. Phys.* **83**, 33 (2011).

11. Radnaev, A. G. *et al*. A quantum memory with telecom-wavelength conversion, *Nature Phys.* **6**, 894-899 (2010).

12. Hau, L. V., Harris, S. E., Dutton, Z. & Behroozi, C. H. Light speed reduction to 17 metres per second in an ultracold atomic gas, *Nature* **397**, 594-598 (1999).

13. Ginsberg, N. S., Garner, S. R. & Hau, L. V. Coherent control of optical information with matter wave dynamics, *Nature* **445**, 623-626 (2007).

14. Zhang, R., Garner, S. R. & Hau, L. V. Creation of long-term coherent optical memory via

controlled nonlinear interactions in Bose-Einstein condensates, *Phys. Rev. Lett.* **103**, 233602 (2009).

15. Simon, C., Riedmatten, H. d. & Afzelius, M. Temporally multiplexed quantum repeaters with atomic gases, *Phys. Rev. A* **82**, 010304 (2010).

16. Rispe, A., He, B. & Simon, C. Photon-photon gates in Bose-Einstein condensates, *Phys. Rev. Lett.* **107**, 043601 (2011).

17. Laurat, J. *et al*. Efficient retrieval of a single excitation stored in an atomic ensemble, *Opt. Exp.* **14**, 6912 (2006).

****

Freestanding, monocrystalline graphene over large apertures in an insulating, solid-state substrate

Principal Investigator: Lene Vestergaard Hau
Faculty Collaborator: Jene A. Golovchenko
Graduate Student: Donald G. Dressen
Graduate Student: Tony X. Zhu

Under this grant we have demonstrated the successful suspension of pristine, single crystals of mono- and multilayer graphene over the largest-area apertures in an insulating substrate ever reported. We have developed a fabrication facility for growing large, single-crystal grains of graphene with chemical vapor deposition. We subsequently transfer graphene from its catalytic-synthesis substrate and suspend it over apertures with

areas as large as ~700 μm2. This is achieved without any modification of the graphene. The graphene synthesis protocol we have developed allows for fabrication of continuous polycrystalline graphene sheets, with large millimeter-sized individual grains. This facilitates scalable fabrication of many suspended graphene devices in parallel.

Earlier observations of large-area suspended graphene have involved fabrication steps that chemically altered the graphene, led to undesirable tearing or contamination, or required metallic support substrates that greatly limited graphene's use in device applications. Our fabricated devices do not suffer from any of these limitations. Moreover, the relative ease with which large numbers of high-quality samples can be simultaneously made are of great importance for the fundamental studies and applications to novel light-matter devices that are pursued in our laboratory as part of this grant.

Background: Graphene is a transparent, highly conductive, two-dimensional material [1]. In addition to its outstanding electrical and thermal conductivities, Gr is the strongest material ever measured [2]. Nevertheless, large areas of freestanding Gr are still fragile and difficult to manipulate because its atomic thinness and its inherent lattice defects leave it vulnerable to macroscopic tearing and rupturing. Additionally, although Gr is very rigid on a molecular scale, it becomes increasingly more pliable on length scales greater than a micron and is prone to folding and rolling up upon itself [3]. For these reasons creating areas of freestanding Gr that are large enough to be experimentally accessible is a formidable challenge and is why Gr has commonly been studied while being placed upon another material. Such supporting substrates can reduce graphene's charge carrier mobility and can also cause uncontrolled doping and change of the Gr

Fermi level [4,5]. Suspended graphene membranes on the other hand are important for microscopic mechanical devices [6], as ion-selective membranes for future filtration applications [7-9], and as dual-side-access substrates for bio-molecular enzymes.

In this project, we successfully suspend pristine mono- and multilayer Gr on an insulating substrate with the largest achievable freestanding areas ever reported. We accomplish this by greatly reducing grain-boundary defects in CVD Gr and by developing enhanced wet and dry transfer methods. Based on recent advances in CVD Gr [10-12], we developed an improved CVD recipe for synthesizing continuous sheets (2 x 7 cm^2) of large grains (1 mm average diameter) of mono- and multilayer Gr. With this advance we demonstrate that membranes can be suspended over arrays of apertures 5-30 μm in diameter (20–700 μm^2) in an insulating SiO_2/Si_3N_4 support substrate. We also demonstrate that both wet and dry transfer methods can be used to create the suspended-Gr membranes, which is of importance for transfer to both hydrophobic and hydrophilic substrates. Furthermore, we show that individual crystals of bi- and trilayer Gr can be successfully suspended over SiO_2/Si_3N_4 apertures up to 30 μm in diameter.

The 700 μm^2 areas of freestanding, pristine mono- and multilayer Gr that we have observed represent the current upper bound for suspended-Gr membranes formed by transferring Gr to an insulating substrate. This is of interest because large areas of freestanding Gr on insulating substrates are especially well suited for electromechanical resonator applications where electrically-isolated, freestanding Gr is essential and where investigators have shown that the resonance frequency and the quality factor of the Gr resonator scale with the resonator's area [13,14]. Gr filtration and desalination devices made from arrays of freestanding membranes will also benefit from larger suspended

areas of pristine Gr that are supported by electrochemically-inert substrates because the flux through such devices depends on both the number of defects in and the overall area of freestanding membranes [7,8,15]. Large-area, freestanding Gr membranes on insulating supports is also important for graphene-based electrochemistry.

Experimental

Graphene synthesis

Continuous sheets of polycrystalline Gr, consisting of single grains between 200-3500 μm in diameter, were synthesized on Cu foils using low-pressure chemical vapor deposition. A strip of 25-μm thick Cu foil (Alfa Aesar, 99.8%), 2 x 7 cm^2 in area, was first washed in 1.0N HCl for 5 min., then sonicated in acetone for 15 min., triple rinsed with isopropyl alcohol, and blown dry with N_2. The strip was then inserted into the center of a quartz tube (22-mm inner diameter, 25-mm outer diameter, 62 cm in length) and slightly bent with a clean glass rod such that the shape of the foil matched the contour of the lower half of the tube but remained 0.5 cm above the bottom surface of the tube. The pressure in the tube was lowered to < 50 mTorr using a scroll pump. Ar (300 sccm) was flowed through the tube for 5 min. after which the pressure in the tube was increased to 750 mTorr using a metering valve located between the end of the tube and the pump. While maintaining an Ar flow rate of 300 sccm, a Lindberg/Blue M Mini-Mite horizontal tube furnace was used to increase the temperature of the system to 1,070°C over a period of 35 min. The Cu foil was annealed at 1,070°C for 5 min. Gr synthesis was begun with the introduction of H_2 and diluted CH_4 (500 ppm in Ar), each at a flow rate of 20 sccm, while the flow rate of Ar was changed to 310 sccm. The synthesis reaction was run for 4 hr. to ensure complete Gr coverage on the bottom side of the copper foil, *i.e.* the side of

the foil facing the bottom surface of the quartz tube. The reaction was arrested by cooling the system for 45 min. using an external fan until the temperature of the furnace was < 30°C. All gases used in the synthesis of Gr were ultra high purity grade.

Substrate fabrication

A Si wafer (<100>; 4" diameter; 500-μm thick) was first cleaned using the standard RCA cleaning protocol. A 300-nm thick layer of low stress (<200MPa) Si_3N_4 was then grown on the top and bottom surfaces of the wafer using low-pressure CVD. Standard photolithography and reactive ion etching (RIE) were used to remove sets of 9 x 12 arrays of squares from the top layer of Si_3N_4, thus exposing the underlying Si in each square. A solution of KOH (40%) was then used to anisotropically etch the exposed Si, forming freestanding Si_3N_4 membranes (250 x 250 μm^2). A second round of photolithography and RIE was done on the freestanding Si_3N_4 membranes to form circular apertures (5, 10, 20, 30, or 50 μm in diameter) at the center of each membrane. After aperture formation, the wafer was thoroughly cleaned using a piranha etch solution. Finally, a 300-nm thick layer of SiO_2 was deposited on top of the aperture-containing Si_3N_4 membranes using plasma-enhanced CVD. All the steps outlined above were completed inside a clean room.

Graphene transfer: wet method

Methyl methacrylate (MMA) polymer solutions (2%, 4%, and 6% MMA in ethyl lactate; diluted from a stock solution of MicroChem 9% MMA 8.5 in ethyl lactate) were each spun on a piece of graphene-containing copper foil (Gr/Cu) for 30 seconds at 3,000 RPM and cured by baking at 180°C on a hot plate for 3 min. To remove Gr on the side of

the Cu foil not covered by MMA, the Gr was etched using O_2 plasma (100W, 1-2 min.). Scissors were then used to cut a piece of the MMA/Gr/Cu stack to fit the size specifications of the target substrate. The copper foil was removed by placing the stack in a bath of ferric chloride solution ($FeCl_3$, Transene CE-100) with the bare Cu side facing down on the solution's surface for 2 hr. to ensure that all the Cu was etched. Once the Cu was completely removed, the MMA/Gr stack was then transferred to a deionized water bath (Millipore, 18MOhms) using a piece of bare Si wafer that had been cleaned using O_2 plasma to make its surface hydrophilic. After several minutes in the water bath, the same piece of Si wafer was used to move the stack to a solution of 1.0N HCl and then to 6 more deionized water baths. While the stack was in the last deionized water bath, it was scooped out using the target substrate (SiO_2/Si_3N_4 chip with an array of 108 apertures), which had previously been O_2 plasma cleaned for 1 min. at 30 W. The MMA/Gr/substrate stack was then placed under a halogen lamp for a minimum of 90 min. to allow the water to migrate out from underneath the stack and to eventually evaporate.

Once dry, the MMA layer was dissolved using acetone at 48°C overnight. Acetone was then exchanged with 200-proof ethanol to facilitate critical point drying. A critical point dryer (Tousimis 931 Series) was used to remove the ethanol. Ethanol was replaced with liquid CO_2 over the course of three, 30 min. cycles. Three slow cycles provided extra assurance that all the ethanol was gently replaced with liquid CO_2 during the drying process.

Graphene transfer: dry method

A 1.5 x 2 cm^2 piece of graphene on Cu foil (Gr/Cu) was first spin coated with 4% (w/w) polymethyl methacrylate (PMMA) in anisole (MicroChem 950PMMA 11 A) for 40 sec. at 1,000 RPM. The PMMA was cured at room temperature for 60 min. Graphene on the backside of the foil was removed by O_2 plasma (100W, 1 min.). The PMMA/Gr/Cu foil stack was then pressed onto the bottom of a 3-mm thick polydimethylsiloxane (PDMS) support frame containing a 1 x 1.5 cm^2 rectangular hole. The Cu foil was etched in ferric chloride ($FeCl_3$, Transene CE-100) for 30 min. then rinsed in deionized H_2O (Millipore, 18MOhm) for 15 min., 2.0N HCl for 30 min., and finally deionized H_2O again for 15 min. A glass microscope slide was used to transfer the PDMS/PMMA/Gr stack between solutions because of the ease at which the suspended PMMA/Gr stack ripped while being pulled off of air/liquid interfaces. After the final deionized H_2O rinse, the stack was lifted out of the solution with a glass microscope slide. Several milliliters of ethanol (200 proof) were then pipetted around the PDMS frame to replace the water trapped underneath the stack with ethanol. This was done to lower the surface tension and help prevent the stack from tearing. The stack was then carefully pulled off the microscope slide so as to avoid tearing the PMMA/Gr and gently blown dry with N_2 for 5 min. A SiO_2/Si_3N_4 substrate with a 9 x 12 array of circular apertures (diameter = 10 or 30 μm) was placed face down on the PDMS/PMMA/Gr stack such that the graphene was in contact with the side of the substrate opposite to that with the pits. The PDMS frame was cut from the PMMA/Gr using a finely pointed scalpel. To promote graphene adhesion the sample was placed in a home-built acetone vapor humidor for 15 min. followed by heating the sample to 180°C for 2 hr. in an atmosphere

of Ar (500 sccm) at a pressure of 500 Torr. The PMMA was thermally removed by heating the sample to 350°C for 4 hr. in an atmosphere of H_2 (500 sccm) and Ar (500 sccm) at a pressure of 1 Torr.

Results

Fabrication of suspended-Gr membranes begins with the synthesis of continuous sheets of large-grain, polycrystalline Gr grown on 25-μm thick copper foils using a home-built low-pressure CVD system. The synthesis protocol we developed is an extension of that described by Zhou *et al* [10]. Several modifications were made to ensure that a continuous sheet of large-grain Gr forms over the entire Cu foil surface. Those modifications include optimizing both the flow rate of the precursor gases and the synthesis reaction time as well as bending the Cu foil such that the bottom of the foil is 0.5 cm from the bottom of the quartz tube during synthesis (see Experimental section above for more details). We found that having the Cu foil in close proximity to the bottom of the tube was critical for forming a continuous Gr sheet on the bottom side of the foil. This is likely because of an increase in Cu vapor pressure and a decrease in gas flow velocity near the tube's wall.

Figure 1 (a)–(d) shows SEM images of groups of hexagonal Gr grains on Cu taken after (a) 30 min., (b) 60 min., (c) 120 min., and (d) 180 min. of synthesis. After 30 min., the majority of grains reach a diameter of 0.3–0.6 mm and fewer than 10% of the grains examined have yet to grow into other grains. By 60 min., most grains are > 1 mm and have started to merge with adjacent grains. After 180 min., Gr covers most of the Cu foil and large Gr islands consisting of individual grains that are between 2–3.5 mm are common. Allowing the reaction to run for 4 hr. gives a continuous sheet of Gr on the

surface of the Cu foil closest to the bottom of the quartz tube. The average grain diameter in the final polycrystalline sheet is estimated to be 0.75–1.5 mm.

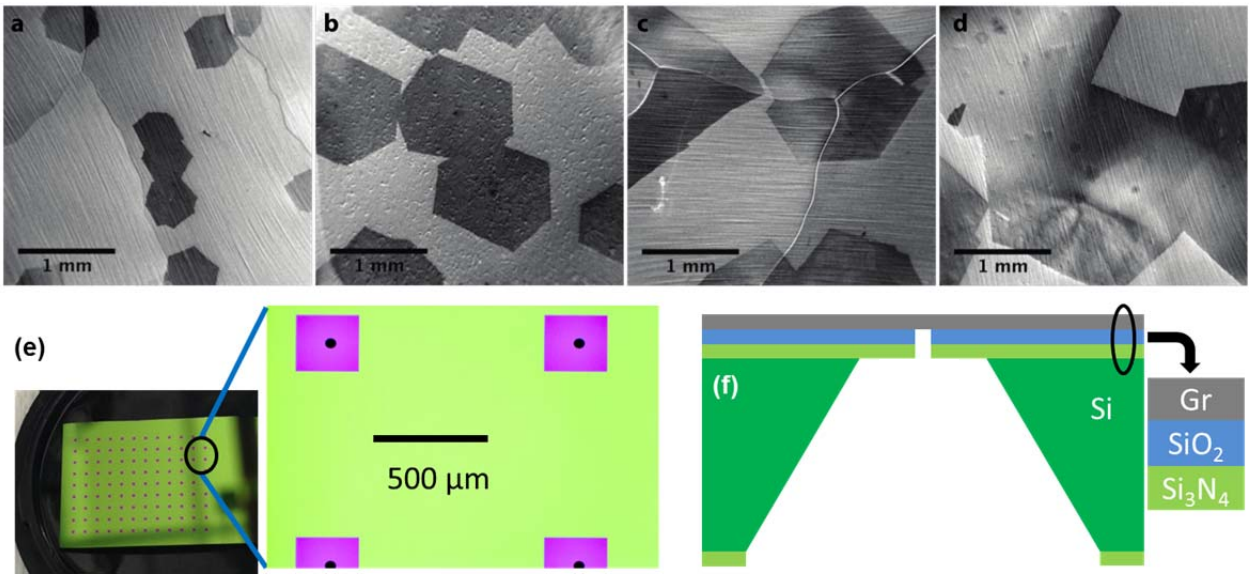

Figure 1. Suspended-Gr membranes. A time series of SEM images reveals the size of hexagonal Gr grains on Cu foil after synthesis times of: (a) 30 min., (b) 60 min., (c) 120 min., and (d) 180 min. A continuous sheet of large-grain, polycrystalline Gr is achieved after 4 hr. Grains can reach diameters of 2–3.5 mm before growing into one another. Small hexagons seen within the larger hexagons of (d) are regions of multilayer Gr. (e) Optical microscope image showing the supporting substrate. The substrate consists of apertures (black circles in the expanded image) in freestanding Si_3N_4 membranes (purple squares) on an underlying Si wafer chip. (f) Cross-section illustration of a suspended-Gr membrane.

Results from optical microscopy, SEM, and Raman spectroscopy analysis of successfully suspended Gr are shown in Figure 2. Figure 2 (a) is a grayscale optical image of Gr suspended over a 30-µm aperture using the wet transfer method. Inside the aperture, the lack of contrast indicates the suspended area is free of tears, particles, large areas of residual polymer contamination, and multiple Gr layers. A single Raman spectrum taken at the center of the aperture is shown in Figure 2 (b). All Raman data were taken with laser excitation photon energy of 2.33 eV at 8 mW and a laser spot size of 1–2 µm. The shape, spectral position, and relative intensity of the G and G' peaks

indicate that the Gr is monolayer. The D peak is nearly absent, confirming that the Gr is pristine with very few defects. For further confirmation of the uniformity of monolayer Gr over the entire aperture, a Raman area scan was taken. Figure 2 (c) shows the resulting map of the Raman shift of the G' peak. Inside the aperture the Raman shift is fairly constant and is centered at 2665 cm^{-1}. Outside the aperture, the presence of the supporting SiO_2/Si_3N_4 substrate causes the G' peak to mostly blue shift to 2675–2680 cm^{-1}, although small regions of red shifting are also observed. These results are typical for most of the membranes that were made.

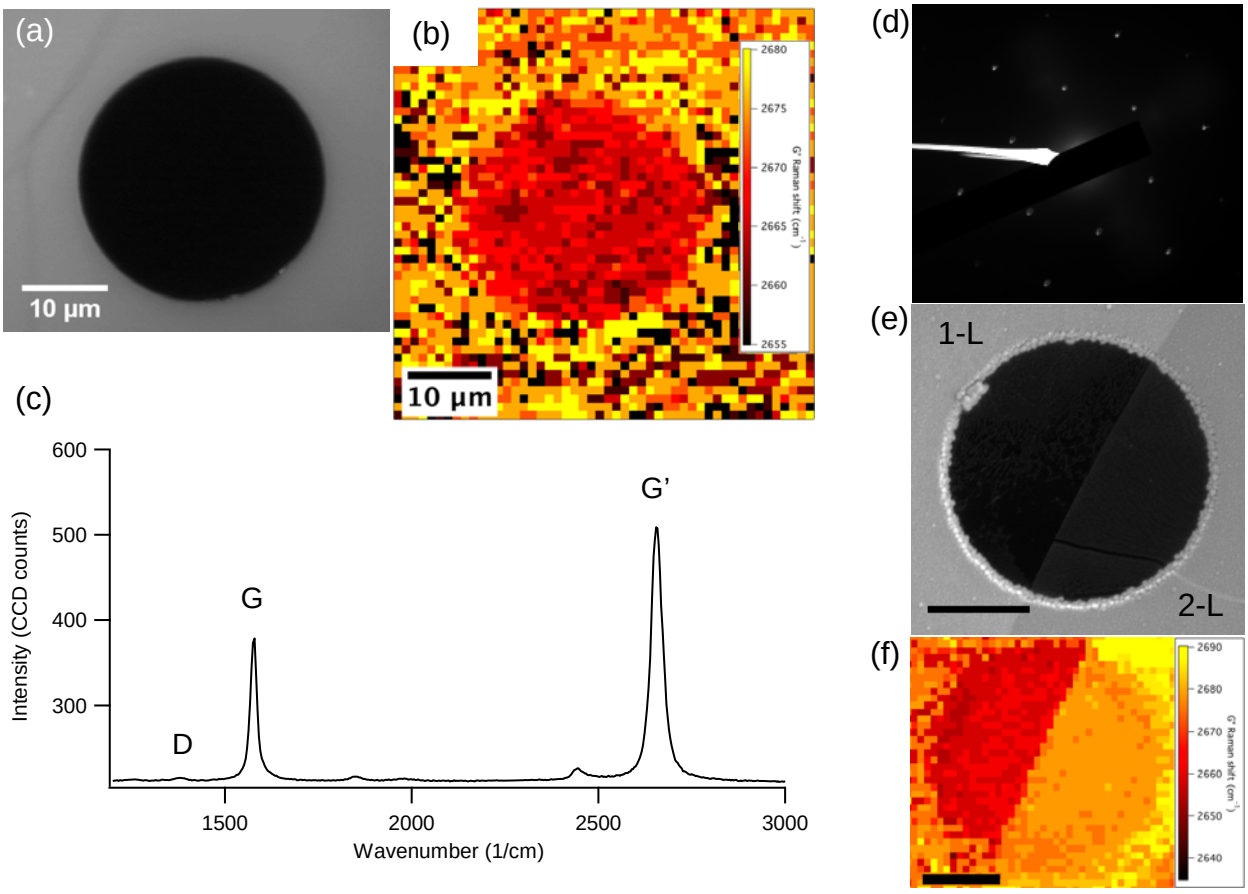

Figure 2. Optical, Raman, SEM, and electron diffraction (ED) analysis of suspended-Gr membranes. (a) Grayscale optical microscope image of freestanding, monolayer Gr over a 30-μm diameter aperture. (b) Spatial Raman map of the same Gr membrane showing the Raman shift of the G' peak over the entire 30-μm aperture. (c) Raman point spectrum taken at the center of the 30-μm aperture. (d) ED pattern of a 10-μm diameter suspended monolayer Gr membrane recorded using a 5-μm spot size (200 kV). (e) SEM

image of a 10-μm diameter suspended-Gr membrane bisected by the edge of a bilayer Gr crystal. 1-L and 2-L denote the Gr layer number (scale bar: 3 μm). (f) Spatial Raman map of the bisected membrane highlighting the difference between the G' peak Raman shift of the monolayer and bilayer regions (scale bar: 3 μm). For the Raman data, laser excitation photon energy = 2.33 eV at 8 mW and laser spot size = 1–2 μm.

With the CVD synthesis protocol we developed we are also capable of forming regions of multilayer Gr, which allows for the fabrication of suspended multilayer Gr membranes. The ability to synthesize multilayer Gr crystals is advantageous because it eliminates both the need to transfer monolayer Gr multiple times to form multilayers and the contamination and defects that multiple transfers produce. The size of the multilayer grains (50–200 μm) as well as the contrast difference on SiO_2 between areas with differing numbers of Gr layers allowed for facile identification of the layer number (up to 5–6 layers) using either optical microscopy or SEM. An example of a 10-μm aperture spanned by both mono- and bilayer Gr is provided in the SEM image of Figure 2 (e). This membrane was created using the dry transfer method and the number of layers has been labeled as 1-L and 2-L. Figure 2 (e) shows that the aperture is bisected by the edge of a bilayer Gr crystal with the left half consisting of monolayer Gr and the right half of bilayer Gr. The lack of particles and residual contamination helps confirm that the membrane is pristine. The line in the lower portion of the bilayer region is likely the result of a fold in the membrane. In the Raman map of Figure 2 (f), which plots the Raman shift of the G' peak over the entire bisected aperture, a clear blue shift is seen when moving from the left monolayer region (2665 cm^{-1}) to the right bilayer region (2675 – 2680 cm^{-1}) as is expected [16,17].

Despite the presence of some multilayer grains containing > 7 layers in the polycrystalline Gr sheets, we observed suspended multilayer Gr membranes with only bi- and trilayers. Figure 3 (a) shows a typical grayscale optical microscope image of a

trilayer region of Gr that is completely spanning a 10-μm aperture (the number of layers has again been labeled as 1-L, 2-L, *etc*.). A comparison of the Raman point spectra of suspended mono-, bi-, and trilayer Gr over separate 10-μm apertures is given in Figure 3 (b). Traces labeled as 'bilayer – a' and 'bilayer – b' represent Raman spectra that were observed for two different and distinct bilayer membranes. The differences in the bilayer spectra are likely caused by differences in the stacking order of the bilayers, as CVD grown Gr often produces bilayers that are randomly rotationally disordered [18,19]. The changes in the G and G' bands for the different Gr types are explicitly shown in Figures 3 (c) and 3 (d), respectively. As expected, the energy and width of the G band change only slightly for the different types of multilayers, with bilayer – b displaying the largest red shift compared to monolayer Gr. The G' band, however, shows appreciable blue shifting and a slight peak narrowing, except in the case of the bilayer – b trace which exhibits a broadening of the G' band.

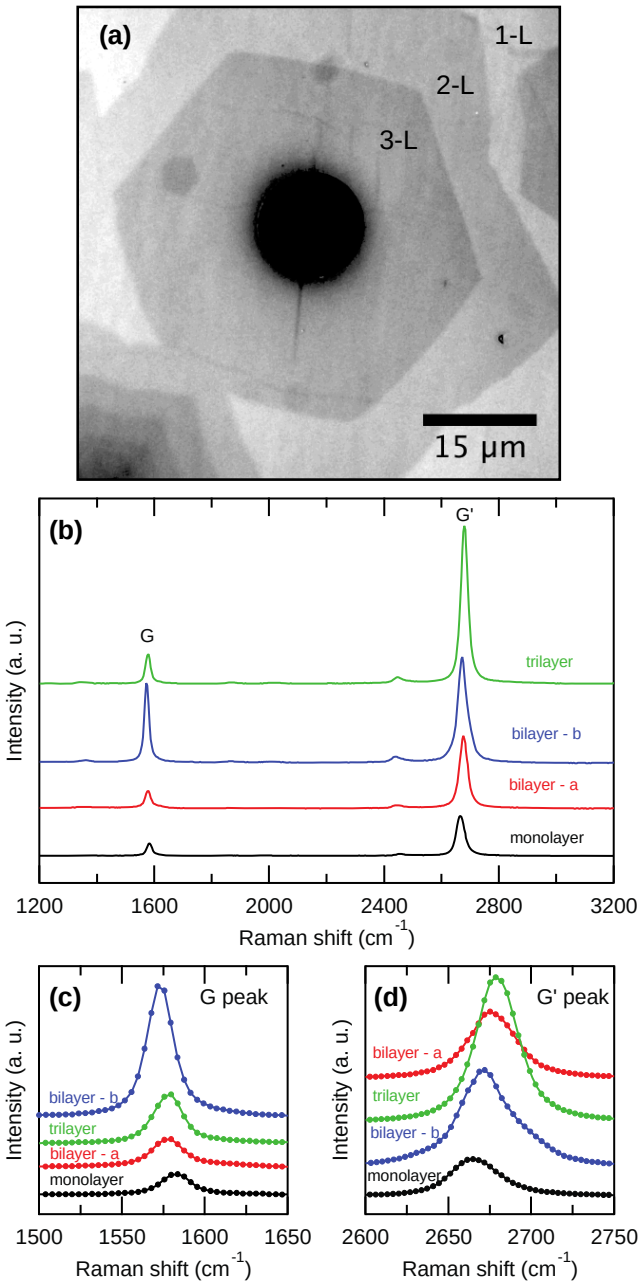

Figure 3. Suspended multilayer Gr membranes and Raman analysis. (a) Grayscale optical microscope image of trilayer Gr suspended over a 10-μm aperture (grayscale used to emphasize contrast difference between Gr layers). 1-L, 2-L, and 3-L denote the Gr layer number. (b) Comparison of Raman point spectra for suspended mono-, bi-, and trilayer Gr. Bilayer – a and bilayer – b are two separate and distinct bilayer membranes, likely exhibiting differing degrees of inter-layer rotational misalignment. The relative changes in the G and G' bands as a function of Gr type are emphasized in (c) and (d), respectively. For the Raman data, laser excitation photon energy = 2.33 eV at 8 mW and laser spot size = 1–2 μm.

References:

[1] Geim, A. K.; Novoselov, K. S. The Rise of Graphene. *Nature Mater.* **2007**, *6*, 183–191.

[2] Lee, C.; Wei, X.; Kysar, J. W.; Hone, J. Measurement of the Elastic Properties and Intrinsic Strength of Monolayer Graphene. *Science* **2008**, *321*, 385–388.

[3] Wolf, E. L. *Applications of Graphene: An Overview*; Springer Briefs in Materials; Springer: New York, 2013; pp. 2.

[4] Bolotin, K. I.; Sikes, K. J.; Jiang, Z.; Klima, M.; Fudenberg, G.; Kim, P.; *et al*. Ultrahigh Electron Mobility in Suspended Graphene. *Solid State Communications* **2008**, *146*, 351–355.

[5] Joshi, P.; Romero, H. E.; Neal, A. T.; Toutam, V. K.; Tadigadapa, S. A. Intrinsic Doping and Gate Hysteresis in Graphene Field Effect Devices Fabricated on SiO_2 Substrates. *J. Phys.: Condens. Matter* **2010**, *22*, 334214, 1–6.

[6] Blees, M.; Rose, P.; Barnard, A.; Roberts, S.; McEuen, P. L. Graphene Kirigami. In Bulletin of the American Physical Society; American Physical Society March Meeting: Denver, CO, 2014; Vol. Volume 59, Number 1.

[7] O'Hern, S. C.; Stewart, C. A.; Boutilier, M. S. H.; Idrobo, J. C.; Bhaviripudi, S.; Das, S. K.; *et al.* Selective Molecular Transport Through Intrinsic Defects in a Single Layer of CVD Graphene. *ACS Nano* **2012**, *6*, 10130–10138.

[8] O'Hern, S. C.; Boutilier, M. S. H.; Idrobo, J. C.; Song, Y.; Kong, J.; Laoui, T.; *et al*. Selective Ionic Transport Through Tunable Subnanometer Pores in Single-Layer Graphene Membranes. *Nano Lett.* **2014**, *14*, 1234–1241.

[9] Joshi, R. K.; Carbone, P.; Wang, F. C.; Kravets, V. G.; Su, Y.; Grigorieva, I. V.; *et al*. Precise and Ultrafast Molecular Sieving Through Graphene Oxide Membranes. *Science* **2014**, *343*, 752–754.

[10] Zhou, H.; Yu, W. J.; Liu, L.; Cheng, R.; Chen, Y.; Huang, X.; *et al*. Chemical Vapour Deposition Growth of Large Single Crystals of Monolayer and Bilayer Graphene. *Nature Communications* **2013**, *4*, 2096, 1–8.

[11] Yan, Z.; Lin, J.; Peng, Z.; Sun, Z.; Zhu, Y.; Li, L.; *et al*. Toward the Synthesis of Wafer-Scale Single-Crystal Graphene on Copper Foils. *ACS Nano* **2012**, *6*, 9110–9117.

[12] Hao, Y.; Bharathi, M. S.; Wang, L.; Liu, Y.; Chen, H.; Nie, S.; *et al.* The Role of Surface Oxygen in the Growth of Large Single-Crystal Graphene on Copper. *Science* **2013**, *342*, 720–723.

[13] Barton, R. A.; Ilic, B.; van der Zande, A. M.; Whitney, W. S.; McEuen, P. L.; Parpia, J. M.; *et al*. High, Size-Dependent Quality Factor in an Array of Graphene Mechanical Resonators. *Nano Lett.* **2011**, *11*, 1232–1236.

[14] Bunch, J. S.; van der Zande, A. M.; Verbridge, S. S.; Frank, I. W.; Tanenbaum, D. M.; Parpia, J. M.; *et al*. Electromechanical Resonators From Graphene Sheets. *Science* **2007**, *315*, 490–493.

[15] Cohen-Tanugi, D.; Grossman, J. C. Water Desalination Across Nanoporous Graphene. *Nano Lett.* **2012**, *12*, 3602–3608.

[16] Jorio, A.; Dresselhaus, M. S.; Saito, R.; Dresselhaus, G. *Raman Spectroscopy in Graphene Related Systems*; John Wiley & Sons: Weinheim, 2011.

[17] Kim, K.; Coh, S.; Tan, L. Z.; Regan, W.; Yuk, J. M.; Chatterjee, E.; *et al*. Raman Spectroscopy Study of Rotated Double-Layer Graphene: Misorientation-Angle Dependence of Electronic Structure. *Phys. Rev. Lett.* **2012**, *108*, 246103, 1–6.

[18] Lenski, D. R.; Fuhrer, M. S. Raman and Optical Characterization of Multilayer Turbostratic Graphene Grown via Chemical Vapor Deposition. *J. Appl. Phys.* **2011**, *110*, 013720, 1–4.

[19] Diaz-Pinto, C.; De, D.; Hadjiev, V. G.; Peng, H. AB-Stacked Multilayer Graphene Synthesized via Chemical Vapor Deposition: a Characterization by Hot Carrier Transport. *ACS Nano* **2012**, *6*, 1142–1148.

****

A new research direction initiated by the results under the NSSEFF grant

Principal Investigator: Lene Vestergaard Hau
Postdoctoral Researcher: John Harrold
Postdoctoral Researcher: Andrew Mutter
Research Assistant: Ray Aubut

We have combined the results and capabilities developed under this grant to pursue a new research direction at the interface of the fields of light-matter interactions, nano-science,

and molecular and synthetic biology. The research involves fundamental studies of light-driven photosynthetic proteins coupled to engineered, inorganic nano-scale structures, and encompasses both natural and gene-engineered proteins. The research defines novel strategies for controlling enzymatic reaction rates, and has applications, for example, for the development of new schemes and devices for light driven bio-fuel production, and for controlling and monitoring enzymatic rates for enzymes of importance for the pharmaceutical industry.

During the last part of this grant, we have in particular developed methods for the controlled positioning of enzymatic molecules on single-layer graphene substrates. Furthermore, graphene's unique properties are utilized and allow for easy control of its redox potential (Fermi level) and, independently, for tuning of the density of available electron states at the Fermi level. This in turn allows for unprecedented control of reaction rates for enzymes positioned on the graphene surface.

The research involves fundamental studies of electron transfer processes at the interface between enzymatic proteins and nanoscale electrodes. For a prototype setup, gene-engineering, based on the methods of synthetic biology, has been applied in our lab for introducing point mutations into Ferredoxin—NADP(+)-reductase (FNR). This protein is expressed in *E. coli* and purified. We have introduced point mutations that result in the insertion of external cystine amino acids at positions of the protein that are close to its redox-active Flavin co-factor. This allows for pyrene attachment and subsequent site-specific Pi-stacking of the enzyme to graphene. We have tested the catalytic activity of these enzymes in solution and verified that the enzymes maintain their enzymatic rates

despite the presence of engineered mutations and pyrene linkers in close proximity to the enzymes' redox-active cofactor.

Most recently, we have attached FNR enzymes to the basal plane both of highly ordered pyrolitic graphite and of single layer graphene. We obtained both excellent reaction rates, and importantly, long-term performance of the enzymes. This sets the stage for experiments where graphene's unique electronic properties can be used for direct control of enzymatic rates in electron transfer reactions for enzymes bound in a single molecular layer on a graphene electrode. A prototype setup has been designed and manufactured where a graphene-based field effect transistor (FET) forms one sidewall in an electrochemical cell that is also equipped with a reference electrode. By next attaching enzymes to the graphene surface, direct measurements of the rates for electron transfer between graphene and the enzyme monolayer can be performed.

In addition, we have designed and built a growth and purification system for isolating macroscopic amounts of the photosynthetic protein PSII. This protein is unique in that it facilitates light-driven water-splitting and occurs naturally in in cyanobacteria and higher plants. We have successfully achieved samples of purified PSII protein that is ready to be interfaced with graphene and tested in a manner similar to that described above for FNR.

Harvard is currently pursuing international patent rights that are based on this research. Furthermore, Harvard has constructed a new laboratory dedicated to the research. The new lab is in addition to our existing optics and nanoscale fabrication labs and allows us to perform the molecular and synthetic biology required for our research. Harvard's building of the new lab was a direct result of this NSSEFF grant and was completed at

the end of 2013. The lab has since been equipped with incubators, centrifuges, and a fast-performance liquid chromatography system.

****

Training of Future Scientists

2 undergraduate students, 6 graduate students, and 8 postdoctoral researchers have been directly supported by this grant. In addition, three more undergraduate students and one graduate student as well as 4 highs school students have been participating in research under this grant.

The research is described on WNYC/NPR's Radiolab:

http://www.radiolab.org/story/267126-master-universe/

AFOSR Deliverables Submission Survey

Response ID:5751 Data

1.

1. Report Type

Final Report

Primary Contact E-mail
Contact email if there is a problem with the report.

hau@physics.harvard.edu

Primary Contact Phone Number
Contact phone number if there is a problem with the report

617-496-8119

Organization / Institution name

Harvard University

Grant/Contract Title
The full title of the funded effort.

Quantum control of light and matter - From the macroscopic to the nano scale

Grant/Contract Number
AFOSR assigned control number. It must begin with "FA9550" or "F49620" or "FA2386".

FA9550-10-1-0208

Principal Investigator Name
The full name of the principal investigator on the grant or contract.

Lene Vestergaard Hau

Program Manager
The AFOSR Program Manager currently assigned to the award

Evelyn Dohme

Reporting Period Start Date

05/01/2010

Reporting Period End Date

10/31/2015

Abstract

During the last part of this grant, we have combined the results and capabilities developed during the grant period to pursue a new research direction at the interface of the fields of light-matter interactions, nano-science, and molecular and synthetic biology. The research involves fundamental studies of light-driven photosynthetic proteins coupled to engineered, inorganic nano-scale structures, and encompasses both natural and gene-engineered proteins. The research defines novel strategies for controlling enzymatic reaction rates, and has applications, for example, for the development of new schemes and devices for light driven bio-fuel production, and for controlling and monitoring enzymatic rates for enzymes of importance for the pharmaceutical industry.

We have developed methods for the controlled positioning of enzymatic molecules on single-layer graphene substrates.

Furthermore, graphene's unique properties are utilized and allow for easy control of its redox potential (Fermi level) and, independently, for tuning of the density of available electron states at the Fermi level. This in turn allows for unprecedented control of reaction rates for enzymes positioned on the graphene surface.

The research involves fundamental studies of electron transfer processes at the interface between enzymatic proteins and nanoscale electrodes. For a prototype setup, gene-engineering, based on the methods of synthetic biology, has been applied in our lab for introducing point mutations into Ferredoxin—NADP(+)-reductase (FNR). This protein is expressed in E. coli and purified. We have introduced point mutations that result in the insertion of external cystine amino acids at positions of the protein that are close to its redox-active Flavin co-factor. This allows for pyrene attachment and subsequent site-specific Pi-stacking of the enzyme to graphene. We have tested the catalytic activity of these enzymes in solution and verified that the enzymes maintain their enzymatic rates despite the presence of engineered mutations and pyrene linkers in close proximity to the enzymes' redox-active cofactor.

Most recently, we have attached FNR enzymes to the basal plane both of highly ordered pyrolitic graphite and of single layer graphene. We obtained both excellent reaction rates, and importantly, long-term performance of the enzymes. This sets the stage for experiments where graphene's unique electronic properties can be used for direct control of enzymatic rates in electron transfer reactions for enzymes bound in a single molecular layer on a graphene electrode. A prototype setup has been designed and manufactured where a graphene-based field effect transistor (FET) forms one sidewall in an electrochemical cell that is also equipped with a reference electrode. By next attaching enzymes to the graphene surface, direct measurements of the rates for electron transfer between graphene and the enzyme monolayer can be performed.

In addition, we have designed and built a growth and purification system for isolating macroscopic amounts of the photosynthetic protein PSII. This protein is unique in that it facilitates light-driven water-splitting and occurs naturally in cyanobacteria and higher plants. We have successfully achieved samples of purified PSII protein that are ready to be interfaced with graphene and tested in a manner similar to that described above for FNR.

Distribution Statement
This is block 12 on the SF298 form.

Distribution A - Approved for Public Release

Explanation for Distribution Statement
If this is not approved for public release, please provide a short explanation. E.g., contains proprietary information.

SF298 Form
Please attach your SF298 form. A blank SF298 can be found here. Please do not password protect or secure the PDF The maximum file size for an SF298 is 50MB.

SF 298 form Hau.pdf

Upload the Report Document. File must be a PDF. Please do not password protect or secure the PDF . The maximum file size for the Report Document is 50MB.

Final Report NSSEFF January 2016.pdf

Upload a Report Document, if any. The maximum file size for the Report Document is 50MB.

Archival Publications (published) during reporting period:

Journal Article:
Hau, L.V. Quantum Optics: Slowing single photons
Nature Photonics 5, 197 (2011)

Patents:
Methods and apparatus for detecting neutral chemical units via nanostructures. Hau, L.V., J.A. Golovchenko, and A. Goodsell, inventors. US Patent #8,729,495, issued May 20, 2014.

Photocatalytic systems comprising graphene and associated methods. Hau, L.V., inventor. Patent Application No. PCT/US2015/024359, filed April 3, 2015.

Changes in research objectives (if any):

Change in AFOSR Program Manager, if any:

Extensions granted or milestones slipped, if any:

AFOSR LRIR Number

LRIR Title

Reporting Period

Laboratory Task Manager

Program Officer

Research Objectives

Technical Summary

Funding Summary by Cost Category (by FY, $K)

	Starting FY	FY+1	FY+2
Salary			
Equipment/Facilities			
Supplies			
Total			

Report Document

Report Document - Text Analysis

Report Document - Text Analysis

Appendix Documents

2. Thank You

E-mail user

Jan 29, 2016 12:55:45 Success: Email Sent to: hau@physics.harvard.edu

Response ID: 5751

Survey Submitted:	Jan 29, 2016 12:55 PM
IP Address:	140.247.113.213

Language:	English (en-US,en;q=0.5)
User Agent:	Mozilla/5.0 (Windows NT 6.1; WOW64; rv:38.0) Gecko/20100101 Firefox/38.0
Http Referrer:	http://afosr.reports.sgizmo.com/s3/
Page Path:	1 : (SKU: 1) 2 : Thank You (SKU: 2)
SessionID:	1454072549_56ab62e5b97a53.15990055

Response Location

Country:	United States
Region:	MA
City:	Cambridge
Postal Code:	02138
Long & Lat:	Lat: 42.380001068115, Long:-71.13289642334